

Modeling and Optimization Analysis of a Single-Flagellum Micro-Structure Through the Method of Regularized Stokeslets

Edgar J. Lobaton and Alexandre M. Bayen, *Member, IEEE*

Abstract—Bacteria such as *Rhodobacter sphaeroides* use a single flagellum for propulsion and change of orientation. These types of simple organisms have inspired microrobotic designs with potential applications in medicine, which motivates this work. In this paper, an elastic model for a single-flagellum micro-structure is presented and followed by an analysis of the system based on optimization. The model is based on the method of Regularized Stokeslets which allows for a discretization of the system into particles connected by spring forces. The optimization analysis leads to the design of an optimal elasticity distribution that maximizes the mean forward speed of the structure. These elasticity coefficients are obtained through the use of adjoint-based optimization. The results are illustrated through simulations showing improvement on the swimming pattern of the micro-structure.

Index Terms—Adjoint optimization, animation and simulation, biologically-inspired robots, microrobotics.

I. INTRODUCTION

HERE have been numerous achievements in MEMS technology which have led to the development of micro-machines such as the ones designed by Donald *et al.* [1] and Yesin [2]. Among some of the main applications for these devices, we find biomedical microrobots capable of performing tasks such as drug delivery [3], diagnosis, and surgical removal of unwanted agents. In this particular paper we present the modeling and design of a micro-structure inspired by single flagellum bacteria.

A bacterial flagellum is a helical structure attached to the body of bacteria which is used for locomotion. Several studies explain the motion patterns observed in bacteria due to chemotaxis and phototaxis. In particular, Armitage and Schmitt [4] describe the type of swimming patterns observed in different bacteria that use flagella for their locomotion. *Rhodobacter sphaeroides* is a particular example of such bacteria, which uses a single flagellum for motion.

Bacteria have a motor at the base of each flagellum which applies a rotational torque. This torque forces the base of the flagellum to rotate. The rest of the structure moves due to the elastic forces joining it together, i.e., there are no internal forces generated in the flagellum (only reactive forces due to

stretching). When the direction of the torque agrees with the handedness of the flagellum, the bacteria moves forward while the flagellum stretches. If the torque is turned off, the flagellum returns to its original position. It is stated in the article [5] by Armitage *et al.* that bacteria such as *Rhodobacter sphaeroides* (*R. sphaeroides*) change direction just by stopping rotation, while other bacteria such as *Escherichia coli* (*E. coli*) reorient themselves by switching the direction of their torques. *R. sphaeroides* are single flagellum organisms while *E. coli* are peritrichously flagellated. For *E. coli*, the dynamics of motion are more complex due to bundling and tumbling motion patterns. Modeling of these processes have been studied by Flores *et al.* [6].

Analysis on the propulsion mechanism of a single flagellum can be found in work by Purcell [7]. However, this type of analysis often ignores the dynamics of the system, any elasticity considerations, and neglects the effect of the body. On the other hand, simulation studies such as the one performed by Flores *et al.* [6] include the dynamics of the system and elasticity of the flagellum. However, the model in [6] does not include the effect of the bacterial body.

The recent years have stressed an increased interest in developing models of swimmers at low-Reynolds number. The interest ranges from biological to nanotechnology applications. For example, a model that uses three spheres for motion was introduced by Najafi and Golestanian [8]. Dreyfus *et al.* [9] built a microscopic artificial swimmer with a flagellum composed of a chain of colloidal magnetic particles linked by DNA. At a macro scale, Long *et al.* [10] built a simple robot that demonstrates the dynamics underlying helical trajectory on microscopic organisms. Previous work has also been done on the motion of solid surfaces using flagellated bacteria as propulsion mechanism by Darton *et al.* [11]. Further work on controlling the motion by using magnetotactic bacteria has been presented by Martel *et al.* [12]. Behkam *et al.* [13] perform a propulsion analysis of a single flagellum in a silicone oil tank, and experiment with an actual array of bacteria for propulsion of larger payloads using chemotaxis for control [14]. Steager *et al.* [15] use phototaxis for motion control. Several efforts have dealt with the study of deformation of helical filaments including the work by Kim and Powers [16]. In their work, bending stiffness is reported to range from $A \approx 10^{-24} \text{ N} \cdot \text{m}^2$ to $A \approx 10^{-21} \text{ N} \cdot \text{m}^2$ and twist modulus in the range $C \approx 10^{-22} \text{ N} \cdot \text{m}^2$ for a variety of filaments in biological structures. Properties of elastic rods in viscous fluids have also been studied experimentally by Qian *et al.* [17] and through intensive numerical simulations using immersed boundary methods by Lim and Peskin [18].

In this paper, the model presented by Flores *et al.* [6] is expanded to reproduce motion of bacteria with a single flagellum such as *R. sphaeroides*. The work is also extended to consider

Manuscript received May 20, 2008; revised October 20, 2008. Manuscript received in final form December 21, 2008. Recommended by Associate Editor F. Caccavale.

E. J. Lobaton is with the Department of Electrical Engineering and Computer Sciences, University of California, Berkeley, CA 94720 USA (e-mail: lobaton@eecs.berkeley.edu).

A. M. Bayen is with the Department of Civil and Environmental Engineering, University of California, Berkeley, CA 94720 USA.

Color versions of one or more of the figures in this brief are available online at <http://ieeexplore.ieee.org>.

Digital Object Identifier 10.1109/TCST.2008.2011889

design strategies for microrobotic applications. The model has been studied and validated for helical structures in the studies of Cortez *et al.* [19] and Flores *et al.* [6]. Hence, we do not go over the particulars of how it incorporates the adequate physical constraints in the system. This model includes a bacterial body and an “engine” that drives the rotation of the structure. The engine can also be thought of as a reacting mechanism to an external field driving the micromachine. The motion for the model is studied, and some key observations on the trajectory of the structure are highlighted. The model uses a combination of closed form solutions of *Stokes’ equations*: the *regularized Stokeslet* and *rotlet*. The model is analyzed: we investigate the influence of the elasticity distribution in the flagellum of the micro-structure on the forward thrust motion. In particular, we characterize an optimum value of the elasticity which provides maximal thrust. This type of analysis can be used for systems biology parameter estimation [20], [21], as well as for design, in particular for micromachines [9], [13], [14], which is a motivation for this work.

We pose the problem of finding an optimal elasticity distribution as an optimization program, in which the underlying flow of the problem (governed by Stokes’ equations) appears in the constraints. We solve this problem with adjoint-based optimization. The specificity of the method proposed in this article lies in the use of the closed form *regularized Stokeslet* and *rotlet* solutions in the computation of the full solution of the direct and the adjoint problems. Adjoint-based control or optimization has proved to be a very efficient technique for shape optimization [22], flow control [23], [24], parameter estimation in biology [20], control of networks [25], [26], inverse modeling, and data assimilation [27]. In most of the adjoint work available in the literature, the gradient of the cost function of the optimization problem is computed explicitly in terms of the solution of the adjoint and the direct problems; note that, the actual numerical solution of the problem has to rely on numerical schemes to solve the corresponding *partial differential equations* (PDEs). In this work, the specific structure of the system enables us to write the gradient explicitly in term of the closed form solutions of Stokes’ equation, which provides an enormous gain in computational efficiency and numerical accuracy.

This paper is organized as follows. First, the model is introduced by reviewing the scheme used for discretization of the structure and displaying some motion results. Then, the adjoint-based optimization analysis is presented by showing the derivations and discussing the implications of our results.

II. MODELING

The model consists of the body, a helical flagellum, and the junction connecting them. The junction, which consists of a hook coming out of the body and attached to the helical flagellum, has at its base the rotor engine that drives the motion. In Section II-B, the engine is modeled by a set of torques. These torques are the active components that drive the motion of the whole structure. The flagellum is a helical-shaped elastic structure that moves due to the forces and torque effects that are imposed on it. Of course, all of these interactions must be computed in a low-Reynolds number environment which is characteristic of the scale of the organism to be modeled.

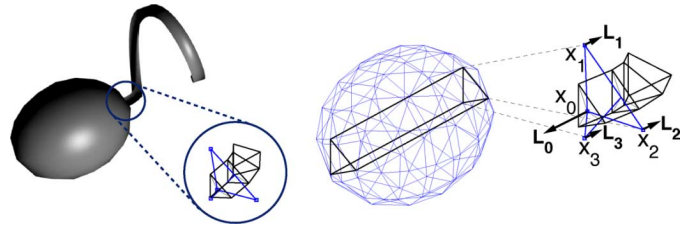


Fig. 1. Rotor and junction structures shown in micro-structure model (left) and as a separate component (right).

The structure is discretized into a set of particles joined by a network of springs (see Fig. 1), which have forces and torques applied to them. The motion of these particles obeys a set of PDEs as it is described in the next section.

A. Particle Method

Due to the low-Reynolds number that characterizes this system, the hydrodynamics of the system can be properly described with the Stokes’ equations

$$\mu\Delta\bar{u} = \nabla\bar{P} - \bar{f}, \quad \nabla\bar{u} = 0 \quad (1)$$

where \bar{u} is the fluid velocity, \bar{P} is the fluid pressure, \bar{f} is the external force density, and μ is the viscosity of the fluid. By proper scaling of the variables by characteristic values of length (\bar{L}) and velocity (\bar{U})

$$x = \frac{1}{\bar{L}}\bar{x}, \quad u = \frac{1}{\bar{U}}\bar{u}, \quad P = \frac{\bar{L}}{\mu\bar{U}}\bar{P}, \quad f = \frac{\bar{L}^2}{\mu\bar{U}}\bar{f} \quad (2)$$

we can obtain dimensionless versions of Stokes’ equations

$$\Delta u = \nabla P - f, \quad \nabla u = 0. \quad (3)$$

These are the equations that will be used to discuss the fluid motion around the flagellum.

For *R. sphaeroides*, the typical length for the flagellum filament is 1–6 μm , and a typical velocity is 10–40 $\mu\text{m}\cdot\text{s}^{-1}$ [5]. Our dimensionless results can be interpreted to a scale comparable to that of *R. sphaeroides* by choosing the factors summarized in Table I. These values were chosen such that the length of the filament in our model (see Table II) corresponds to 2 μm , and the maximum velocity observed in Fig. 4 is close to 20 $\mu\text{m}\cdot\text{s}^{-1}$.

Here we use the *regularized Stokeslet* and *regularized rotlet* solutions used by Flores *et al.* [6], introduced by Cortez *et al.* [19], for the cases of a single point force f_0 and a single point torque L_0 applied at location x_0 . The method of regularized Stokeslet has been validated for the use of helical structures by Cortez *et al.* [19]. Also, Flores *et al.* [6] show more comparisons to biological data for *E. coli*.

The *regularized Stokeslet* and *rotlet* solutions are given by

$$\begin{aligned} U_s(x; x_0, f_0) &= \frac{(r^2 + 2\delta^2)}{8\pi(r^2 + \delta^2)^{3/2}}f_0 + \frac{[f_0^T(x - x_0)]}{8\pi(r^2 + \delta^2)^{3/2}}(x - x_0) \\ U_r(x; x_0, L_0) &= \frac{(2r^2 + 5\delta^2)}{16\pi(r^2 + \delta^2)^{5/2}}[L_0 \times (x - x_0)] \end{aligned} \quad (4)$$

where r is the distance between x and x_0 , and δ is the regularizing parameter in the method. These formulas express analytical solutions to a regularized version of the Stokes (3) in

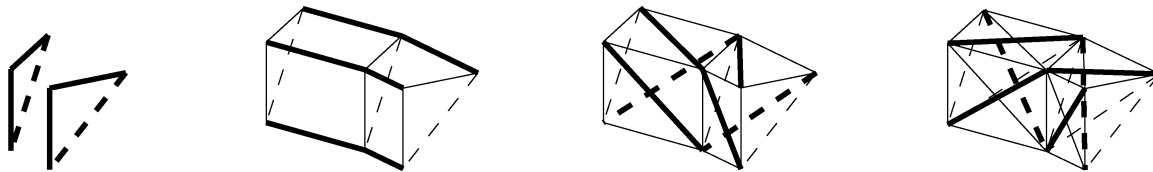


Fig. 2. There are four types of springs on the flagellum: cross sectional, longitudinal, diagonal, and anti-diagonal (from left to right). For each triangular cross section there are three cross sectional springs. Going along the flagellum, we can group these springs into three components. We can similarly obtain three components for each one of the spring categories mentioned before.

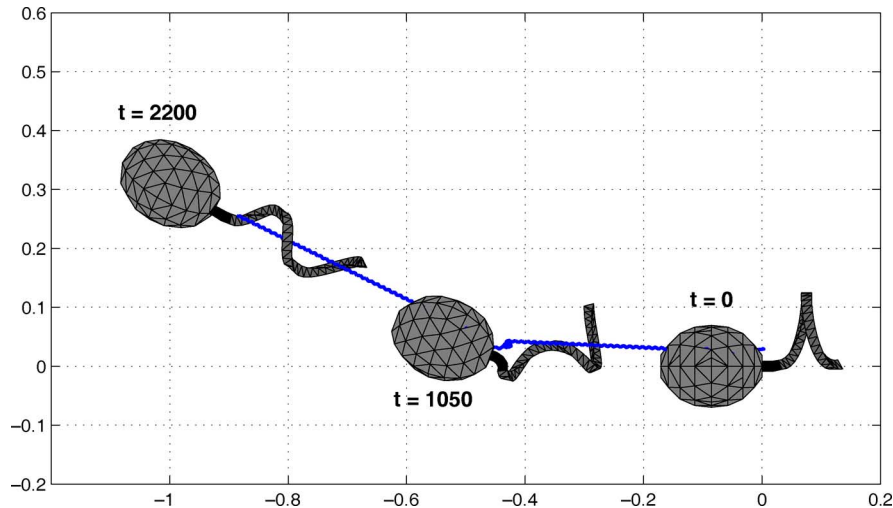


Fig. 3. Motion simulation illustrating change of orientation due to reversing the torque at $t = 1000$ for a duration of 30 units of time. The path followed by average particle is shown as a solid curve.

TABLE I
CONVERSION FROM DIMENSIONLESS TO DIMENSIONAL UNITS

| Dimensionless variable | Factor |
|-------------------------|--|
| Length | $\bar{L} = 5 \cdot 10^{-6} m$ |
| Velocity | $\bar{U} = 10^{-1} m s^{-1}$ |
| Viscosity μ (water) | $\mu = 10^{-3} kg m^{-1} s^{-1}$ |
| Time | $\bar{T} = \bar{L}/\bar{U} = 5 \cdot 10^{-5} s$ |
| Force density | $\bar{F} = \mu\bar{U}/\bar{L}^2 = 4 \cdot 10^6 N m^{-3}$ |
| Torque density | $\bar{T}_q = \mu\bar{U}/\bar{L} = 20 N m^{-2}$ |

TABLE II
GEOMETRIC PARAMETERS (IN DIMENSIONLESS UNITS)

| Parameter | Value |
|---|-------|
| Length of axis of body in x -direction (a_x) | 0.09 |
| Length of axis of body in yz -directions (a_{yz}) | 0.07 |
| Number of particles for discretization (N_H) | 75 |
| Radius of curvature of junction (R_J) | 0.02 |
| Number of triangular cross sections in junction (N_J) | 5 |
| Radius of tubular region around centerline of junction (r) | 0.01 |
| Amplitude of flagellum (R_F) | 0.06 |
| Wavelength of flagellum (α) | 0.1 |
| Arc-length of flagellum (L_F) | 0.4 |
| Number of triangular cross sections in flagellum (N_F) | 30 |
| Radius of tubular region around centerline of flagellum (r) | 0.01 |

which the forces and torques are not applied at single points, but are distributed over a small neighborhood of the application point. For more details refer to [6]. Throughout this brief, we

use $\delta = 0.02$ which is consistent with the size of our discretization. This choice is made based on numerical arguments present in [6] and [19].

Common Stokeslet and rotlet solutions to the application of point forces and torques in a system governed by the Stokes equations yield singular solutions. This would make the formulation of the optimization of a functional based on these solutions problematic due to the lack of differentiability of the solution. The method of regularized Stokeslet yields smooth versions of these solutions, which allows the application of the calculus of variations. Also, having control over a regularization parameter can lead to the use of multiscale schemes for the optimization of our objective functional.

These closed form solutions give us a velocity field that can be used to track particles moving in the fluid. Hence, we only require a model that specifies the forces and torques due to a particular configuration at a specified time. In this model, the effect of the forces (which are defined at all particle locations) and the torques (applied at a total of four locations) can be combined to define the following dynamics for the system of particles indexed by k :

$$\dot{x}_k = \sum_{i=0}^3 U_r(x_k; x_{n_i}, L_i) + \sum_{j=1}^{N_x} U_s(x_k; x_j, f_j) \quad (5)$$

where $R \triangleq \{n_i\}_{i=0}^3$ is the set of indices where torques $\{L_i\}$ are applied, f_j is the force applied at point x_j , and N_x is the total number of particles. See Fig. 1 and Section II-B for an illustration.

B. Model

The model follows the methodology developed by Flores *et al.* [6]. The flagellar structure and the body are discretized into a collection of particles with a network of springs connecting them. A view of some of these connections is shown in Figs. 1 and 2.

Our model consists of an ellipsoid representing the body, a tubular section with a helical centerline representing the flagellum, and a tubular section with part of a circular centerline representing the hook that joins the body to the flagellum. The equation for the body is given by

$$\frac{(x + a_x)^2}{a_x^2} + \frac{y^2}{a_{yz}^2} + \frac{z^2}{a_{yz}^2} = 1$$

where a_x and a_{yz} are the length of the axis of the ellipsoid. The equation is shifted so it matches properly with the hook. The equation for the centerline of the hook is

$$(x, y, z) = (R_J \sin(s), R_J(1 - \cos(s)), 0), \quad s \in \left[0, \frac{\pi}{2}\right]$$

where R_J is the radius of curvature of the junction. Finally, the equation for the centerline of the flagellum is

$$(x, y, z) = \left(\alpha \frac{s}{(2\pi)}, R_F \sin(s) + R_J, R_F(1 - \cos(s)) \right)$$

where $s \in [0, L_F/\sqrt{\alpha^2 + R_F^2}]$, R_F is the amplitude of the helix, α is the wavelength of the helix, and L_F is the total arc-length of the helix. The tubular sections around the centerlines for the hook and the flagellum have radius r . For our discretization, we consider triangular cross sections normal to the tangent of the centerlines for the flagellum and the hook. A total of N_J cross sections and N_F cross sections are considered for the junction and the flagellum, respectively. The body is discretized by considering particles along circles normal to the x direction. A total number of N_H particles are used for discretizing the whole surface of the body.

The values used in our simulations are given in Table II. Fig. 1 shows a 3-D rendering of our model for the given parameters.

The particles and spring connections on the body define a triangular tessellation of its surface. Besides having spring connections on the surface of the body, we also define connections between the front and back particles in the body. These are marked with dark lines in the right plot of Fig. 1. These connections are there to make the structure more stable.

The flagellum is discretized by using triangular cross sections perpendicular to the helix that determines the centerline of the structure. The types of spring connections in the flagellum are cross sectional, longitudinal, diagonal, and anti-diagonal. Fig. 2 illustrates these connections with the darker lines corresponding to each set of connections.

The body is joined to the flagellum by a junction shaped as a hook. This junction is discretized in the same way as the flagellum. The junction is connected to the body through the rotor engine. This engine is discretized allowing for free rotation of the junction. On the right plot of Fig. 1 the engine structure (which is a diamond-like structure joined to the body) and part of the junction are shown. The left plot of Fig. 1 shows these components and their location in the model.

Forces due to the stretching of a spring are defined by using Hooke's law. The total force at a particle location x_j is the summation of the forces due to all the particles connected to it, and it is given by

$$f_j = \sum_{n \in c(j)} \alpha_{jn} \left(1 - \frac{r_{0,jn}}{r_{jn}}\right) (x_n - x_j) \quad (6)$$

where $c(j)$ is the set of indices of particles connected to x_j by spring, α_{jn} is the elasticity of the spring connection between x_j and x_n , r_{jn} is the distance between the particles, and $r_{0,jn}$ is the rest length of the corresponding spring.

The driving forces in the engine are the torques. A main torque L_0 is applied at location x_{n_0} , and counter-torques L_i are applied at locations x_{n_i} for $i = 1, \dots, 3$. The location of the torques are shown in the right plot of Fig. 1. All of these torques are defined to be parallel. The magnitude σ_0 of the main torque is given by σ (a parameter chosen for the simulation), and the magnitude σ_i of the counter-torques is given by $-\sigma/3$ which is chosen to conserve angular momentum. For all of our simulations, we chose $\sigma = 0.001$. The equation of any of the torques is given by

$$L_i = \sigma_i \frac{p}{\|p\|} \quad (7)$$

where $p \triangleq (x_{n_0} - (x_{n_1} + x_{n_2} + x_{n_3})/3)$. The vector p points in the same direction as the tangent to the axis of rotation of the junction. The locations of the points x_{n_i} in our structure are shown in Fig. 1.

C. Motion Results

For this section, elasticity values were chosen to be: 20 on the body, 60 on the junction, and 40 on the flagellum. Note that all types of coefficients (i.e., cross sectional, longitudinal, diagonal, and anti-diagonal) are given the same values for the junction and the flagellum.

Fig. 3 shows the position and configuration of the model at different stages of the simulation. For this simulation, the torque is turned-on at time $t = 0$, its direction is reversed at time $t = 1000$, and it is set again to its original magnitude at $t = 1030$. Initially the flagellum has a small pitch (top-left). As the structure moves, the flagellum stretches (top-right). The structure changes orientation when the torque is reversed (middle-left), and reorients itself (middle-right) when the torque is reset. Finally, the structure moves in a new direction (bottom-right) with a change of orientation of about 30 deg. It is observed that the applied torque acts as a 1-DOF actuator for changing the swimming direction of the structure. This actuator uses the passive properties of the flexible flagellum and provides an avenue for trajectory tracking. Animations of the motion can be seen at: <http://www.eecs.berkeley.edu/~lobaton/Bacteria/index.html>.

III. ADJOINT-BASED SPEED OPTIMIZATION

The goal of this section is to analyze the elasticity distribution over the flagellum. In particular, we compute an elasticity distribution of the flagellum which maximizes the average forward velocity. A gradient descent algorithm will be used next to obtain the minimum of a functional that is specified below and encodes average velocity. The derivation of the gradient is

performed using the adjoint problem, since a direct computation using finite difference would be computationally too expensive and potentially inaccurate.

A. Optimization Problem With PDE Constraints

We formulate the problem as a constrained optimization program. We aim to find the optimal elasticity distribution over the flagellum that maximizes the mean forward speed of our structure given that the dynamics are constrained by the Stokes' equations (3).

Due to the complex motion of the structure, the mean forward speed v is not a quantity that can be expressed in closed form. However, it can be approximated by considering the average distance traveled by a particle k , i.e.,

$$v \approx \frac{\|x_k(T) - x_k(0)\|_2}{T}.$$

This is a valid approximation for large enough T . Hence, the following objective functional is defined from considering the distance traveled by the average among all particles

$$J(\alpha) = \frac{-\left(\frac{\|\bar{x}(T;\alpha) - \bar{x}(0;\alpha)\|_2}{T}\right)^2}{2} \quad (8)$$

where $\bar{x}(t; \alpha) = \sum_{i=1}^{N_x} x_i(t; \alpha)/N_x$, α encodes the design parameters (in our case, the elasticity distribution over the flagellum), and N_x is the number of particles in the structure. The dependency of the trajectories on α is emphasized by using the notation $x_i(t; \alpha)$. The average among all particles can be thought as a center of mass computation. Technical reasons as of why this average particle is used, instead of focusing on a single particle, will be given later. The design parameter α only appears explicitly on the computation of the forces between particles as seen in Section II-B. In turn, these forces specify the velocity flow field that updates the position of the particles.

Therefore, the optimization problem is posed as the minimization of the objective functional given in (8) with constraints given by (5), where the forces and torques are defined by the current configuration of the structure.

B. Considerations due to Periodic Configuration

Due to the physical nature of the motion, it is expected to find periodic behavior associated with the configuration of the structure. This is also observed in the numerical simulations. Hence, it can be assumed that the motion of a particle is of the form

$$x_k(t) = x_k(0) + vt\hat{e}_1 + p_1(t)\hat{e}_1 + p_2(t)\hat{e}_2 + p_3(t)\hat{e}_3 \quad (9)$$

where $p_i(t)$ are periodic functions of period τ and $p_i(0) = 0$, \hat{e}_1 is the unit vector in the direction of the mean velocity, and $\{\hat{e}_i\}$ form an orthonormal basis. This implies

$$\frac{\|\bar{x}(T) - \bar{x}(0)\|_2^2}{T^2} = v^2 + O\left(\frac{1}{T}\right).$$

Using this result and (8), then

$$J(\alpha) = \frac{-v^2}{2} + O\left(\frac{1}{T}\right).$$

Note that if $T \triangleq N\tau$, where N is an integer and the motion is exactly periodic, then the last term vanishes. However, using this for the adjoint computation would require knowing τ explicitly as a function of α . In order to reduce the last term in the functional evaluation, T is computed such that $T \approx N\tau$ by minimizing the L_2 difference between configurations after some fixed time.

From the previous equation, it also follows that

$$D_\alpha J(\alpha) = -v^T(D_\alpha v) + O\left(\frac{1}{T}\right).$$

In this case, the last term does not vanish for $T = N\tau$, but the right-hand side becomes a better estimate to $-v^T(D_\alpha v)$ as $T \rightarrow \infty$. The latter is of interest since the goal is to maximize the mean forward speed.

C. Adjoint Derivation

By perturbing the system and noting that the i th elasticity coefficient α_i (here we are assuming an ordering of the coefficients) only appear explicitly in the computation of the forces, we have

$$\begin{aligned} \dot{x}'_k &= \sum_{i=0}^3 (D_1 U_r(x_k; x_{n_i}, L_i) x'_k \\ &\quad + D_2 U_r(x_k; x_{n_i}, L_i) x'_{n_i} + D_3 U_r(x_k; x_{n_i}, L_i) L'_i) \\ &\quad + \sum_{j=1}^{N_x} (D_1 U_s(x_k; x_j, f_j) x'_k + D_2 U_s(x_k; x_j, f_j) x'_j \\ &\quad + D_3 U_s(x_k; x_j, f_j) f'_j) \\ L'_i &= \sum_{m \in R} (D_{x_m} L_i) x'_m \\ f'_j &= \sum_{m=1}^{N_x} (D_{x_m} f_j) x'_m + \sum_{n=1}^{N_\alpha} (D_{\alpha_n} f_j) \alpha'_n \end{aligned} \quad (10)$$

where it is assumed that the first N_α elasticity coefficients are the ones used for the optimization, D_i stands for the gradient with respect to the i th entry, and $\{x'_k, f'_k, L'_k\}$ are the corresponding first order variations. By recombining all of these terms the previous equation can be expressed as

$$\begin{aligned} \dot{x}'_k(t) &= \sum_{i=1}^{N_x} F_{k,i}(S(t)) x'_i(t) + \sum_{j=1}^{N_\alpha} G_{k,j}(S(t)) \alpha'_j \\ x'_k(0) &= 0 \end{aligned} \quad (11)$$

where $S(t)$ stands for the configuration of the structure at time t . Definitions and explicit formulations of $F_{k,i}$, $G_{k,j}$ are given in Appendix A. The first variation of the energy functional given in (8) is given by

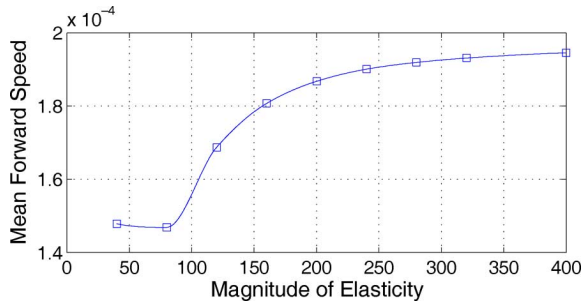


Fig. 4. Mean forward speed results (in dimensionless units) when varying magnitude of the constant uniform distribution for the elasticity.

$$J'(\alpha) = - \left(\frac{1}{(N_x T^2)} \right) \sum_{i=1}^{N_x} (\bar{x}(T) - \bar{x}(0))^T x'_i(T). \quad (12)$$

The adjoint state $y_k(t)$ is defined in order to obtain an analytical expression in terms of α'_k . Multiplying both sides of (11) by the transpose of the corresponding adjoint state and integrating over time, then

$$\begin{aligned} \int_0^T y_k^T(t) \dot{x}'_k(t) dt &= y_k^T(T) x'_k(T) - \int_0^T \dot{y}_k^T(t) x'_k(t) dt \\ \int_0^T y_k^T(t) \dot{x}'_k(t) dt &= \int_0^T y_k^T(t) \sum_{i=1}^{N_x} F_{k,i}(S(t)) x'_i(t) dt \\ &\quad + \int_0^T y_k^T(t) \sum_{j=1}^{N_\alpha} G_{k,j}(S(t)) \alpha'_j dt. \end{aligned}$$

A summation over all particles of the structure provides

$$\begin{aligned} \sum_{k=1}^{N_x} y_k^T(T) x'_k(T) &= \sum_{i=1}^{N_x} \int_0^T \dot{y}_i^T(t) x'_i(t) dt \\ &\quad + \sum_{i=1}^{N_x} \int_0^T \sum_{k=1}^{N_x} y_k^T(t) F_{k,i}(S(t)) x'_i(t) dt \\ &\quad + \sum_{j=1}^{N_\alpha} \int_0^T \sum_{k=1}^{N_x} y_k^T(t) G_{k,j}(S(t)) \alpha'_j dt \\ \sum_{k=1}^{N_x} y_k^T(T) x'_k(T) &= \sum_{i=1}^{N_x} \int_0^T \left(\dot{y}_i^T(t) + \sum_{k=1}^{N_x} F_{k,i}^T(S(t)) y_k(t) \right) x'_i(t) dt \\ &\quad + \sum_{j=1}^{N_\alpha} \left(\int_0^T \sum_{k=1}^{N_x} G_{k,j}^T(S(t)) y_k(t) dt \right) \alpha'_j. \end{aligned}$$

The following definition:

$$\dot{y}_i(t) = - \sum_{k=1}^{N_x} F_{k,i}^T(S(t)) y_k(t) \quad y_i(T) = \bar{x}(T) - \bar{x}(0)$$

when incorporated in the previous formula, can be used to express (12) as follows:

$$J'(\alpha) = - \frac{1}{N_x T^2} \sum_{j=1}^{N_\alpha} \left(\int_0^T \sum_{k=1}^{N_x} G_{k,j}^T(S(t)) y_k(t) dt \right) \alpha'_j.$$

We note that in the previous derivations, it is essential to have a summation over the index k in order to obtain the desired simplifications. This summation comes from the consideration of the average particle in our functional. This is the reason why the functional is based on the displacement of the average particle instead of focusing on a single particle. By defining

$$\begin{aligned} z_k(t) &\triangleq y_k(T-t), \\ \bar{F}_{k,i}(t) &\triangleq F_{k,i}^T(S(T-t)) \quad \text{and} \\ \bar{G}_{k,j}(t) &\triangleq G_{k,j}^T(S(T-t)) \end{aligned} \quad (13)$$

the previous equations become

$$\begin{aligned} \dot{z}_i(t) &= \sum_{k=1}^{N_x} \bar{F}_{k,i}(t) z_k(t) \quad z_i(0) = \bar{x}(T) - \bar{x}(0), \\ J'(\alpha) &= - \frac{1}{N_x T^2} \sum_{j=1}^{N_\alpha} \left(\int_0^T \sum_{k=1}^{N_x} \bar{G}_{k,j}(t) z_k(t) dt \right) \alpha'_j. \end{aligned} \quad (14)$$

Hence, it is possible to identify the gradient of the cost functional as

$$\frac{\partial J}{\partial \alpha_j}(\alpha) = - \frac{1}{N_x T^2} \int_0^T \sum_{k=1}^{N_x} \bar{G}_{k,j}(t) z_k(t) dt. \quad (15)$$

This result can now be used in any gradient descent algorithm (as it is also illustrated in [20], [26], and [28]) to minimize the desired functional. Our particular implementation performs a linear search on the direction of the gradient. We constraint our linear search to the close interval for which the design parameter α remains with positive components (since negative elasticity does not make physical sense).

D. Optimization Results

For this section and the following, we use the same elasticity values as specified in Section II-C. The values given to the elasticity of the flagellum are the ones over which we will optimize, with an initial value of 40 for all of them.

As described in Section II-B, the flagellum is discretized using triangular cross sections perpendicular to the helix centerline of the structure. The spring connections defined can be categorized into four types (see Fig. 2): cross sectional (between particles in the same cross section), longitudinal (between corresponding particles in the following cross section), diagonal and anti-diagonal (between any other particles in the following cross section that has not been connected yet). We distinguish between three components in each category due to triangular cross sections in our model.

For the optimization process, each of these types of spring connections are initialized to the value of 40 uniformly. Then, updates are done based on a particular search direction. This initial value was chosen to yield a steady forward motion. Any elasticity value less than 40 did not end up in steady forward motion during simulation.

1) *Using Constant Uniform Distributions*: In order to have a basis of comparison for the optimization results using the previous gradient computation, we look for the optimal mean forward speed over the space of constant uniform distribution (i.e., so the elasticity remains constant throughout the flagellum). In

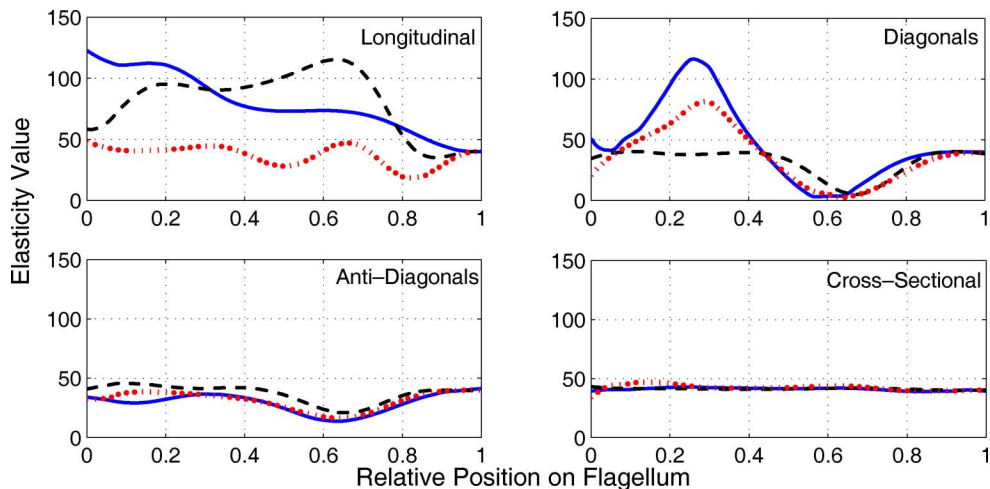


Fig. 5. Plots of the elasticity components along the flagellum for the optimal distribution found. The x -axis depicts the relative position along the arc-length of the flagellum where 0 is at the base and 1 is at the end. The y -axis is the elasticity value. Due to triangular cross sections, there are three components for each elasticity category. These components are illustrated in Fig. 2.

TABLE III
PATH STATISTICS FOR MEAN PARTICLE (IN DIMENSIONLESS UNITS)

| Category | Optimal | Initial | Ratio |
|--------------------------|-----------------------|-----------------------|-------|
| Mean Forward Speed | 5.27×10^{-4} | 1.48×10^{-4} | 3.56 |
| Frequency of Oscillation | 4.0×10^{-2} | 3.7×10^{-2} | 1.08 |
| Amplitude of Oscillation | 2.0×10^{-3} | 1.3×10^{-3} | 1.54 |

this case, we have only one free parameter, which is the magnitude of the elasticity.

By varying the magnitude of the elasticity, we expect that for low values (weak springs) the structure will not be able to hold its shape properly causing slower speed. Ultimately if the elasticity is 0, there should be no forward speed. The other extreme is having a high value for the elasticity (strong springs). In this case, we expect that the structure will keep its initial configuration. We expect in this case to have more of a rigid body motion and with a finite forward velocity (i.e., we expect the velocity to converge to a value for high elasticity values). Fig. 4 shows the mean forward speed for an elasticity value in the interval 40 to 400. This function plot was obtained by sampling the function at marked locations. No values smaller than 40 were used because the flagellum would not be able to get to a stable configuration with these values. As expected this plot shows the mean forward velocity values converging for high values of elasticity. We estimate this final velocity to be about 2×10^{-4} , which is about 1.35 times our initial speed. Hence, this optimization process yields an improvement of 35%. We now compare these results with the optimization using the gradient information.

2) *Using Gradient Descent:* In this section, the gradient is computed using (14)–(15), and then used to update the elasticity coefficients by gradient descent. The optimal step size is obtained by linear search on the direction of the gradient. At the end of the optimization, the optimal distribution yields a mean forward speed of over 3.5 times the original speed as it is shown in Table III. This is about 2.6 times better than the optimal increase obtained from the constant distribution case in the previous section.

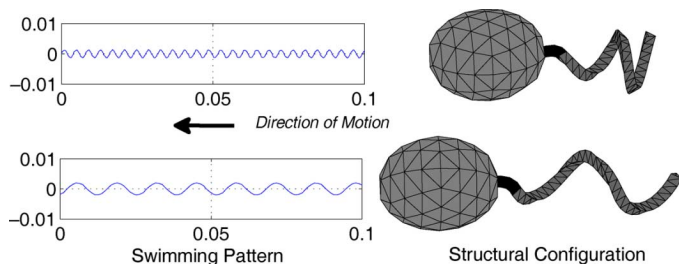


Fig. 6. Comparison between swimming patterns (left) and corresponding structural configurations (right). Trajectories on the xy plane of the average particle before optimization (top-left) and after (bottom-left) are compared. The scale in the configuration plots is five times the scale in the trajectories.

In Fig. 5, the elasticity distribution for the different components along the flagellum after convergence of the algorithm is shown. We observe an overall increase on the longitudinal coefficients from their initial value of 40. Since the longitudinal springs have the effect of maintaining the length of the flagellum constant, we could conclude that the optimal distribution does not allow for stretching of the flagellum. This is validated in our simulations by noting a minimal change on the arc-length of the flagellum in the order of 1%. For the diagonal coefficients we observe that the springs are strengthened at locations in the flagellum closer to the body and weakened at locations farther away from the body. Since the diagonal springs can be associated to the amount of torsion allowed in the structure, the optimal distribution allows for more torsion at locations farthest from the body. This can be seen clearly by comparing the configuration at the right of Fig. 6. Weakening the diagonal springs yields more torsion on the structure, which translates into a longer amplitude at the end of the flagellum that is farthest from the body, as observed by comparing the configurations before (top-right) and after (bottom-left) optimization. We also observe an overall decrease for the anti-diagonal coefficients, and small variations for the cross sectional values.

Since the optimization involves the estimation of the velocity of the average particle, it is useful to analyze the trajectory this

average particle follows. In Fig. 6, we observe two trajectories in the xy -plane. The trajectory for the initial uniform distribution is shown on top. The trajectory for the optimal distribution is shown at the bottom. It is observed that there is no noticeable change on the frequency of oscillation on these helical paths. This is true despite the change on the wavelength and amplitude of the paths. Some statistics comparing these two paths are shown in Table III.

There is also a noticeable difference between the configurations of the structure during motion. On the top-right of Fig. 6, the plot shows a configuration of the structure during motion before any gradient update is applied. On the bottom-right of the same figure, a configuration during motion after optimization is shown. There is a noticeable increase on the pitch of the helical structure at the end of the flagellum that is furthest from the body.

IV. CONCLUSION AND FUTURE WORK

This paper derives a mathematical framework to model the structural properties of a flagellum, and the corresponding swimming patterns in low Reynolds number flows. The motion modeling portion of this work successfully simulates bacterial forward motion and change of orientation by reversing the torque for a single-flagellum organism. For the optimization part of this brief, the aim was to maximize the forward speed in terms of the elasticity distribution on the flagellum. An explicit expression for the gradient of a cost functional encoding forward speed of the flagellum was obtained using the adjoint method. This estimate of the gradient was also successfully used for computing elasticity distributions that yield higher speed. Also, the observed conformation of our model matched what was expected from biological observations. This analysis can easily be extended to optimizing structural shape of the flagellum.

Due to the regular structure of flagella in biological organisms, the types of elasticity distributions presented in this work are not a feature which biological organisms can necessarily achieve by themselves. Also, elasticity properties of biological structures are very sensitive to environmental parameters such as pH level and temperature. However, the fabrication of nanoscale filaments with any desired elastic properties can be foreseen in the near future; with numerous applications in microrobotics.

The model can be improved by including other boundary conditions that are more suitable such as planes with no-slip boundary conditions for direct comparison to biological data

and experimental results such as the ones presented by Behkam *et al.* [13], which we hope to do in the future.

APPENDIX A

COMPUTING $F_{k,i}$ AND $G_{k,j}$

By identifying the coefficient of α'_n in (10) to the coefficients in (11), it can be observed that

$$\sum_{n=1}^{N_\alpha} G_{k,n}(S(t))\alpha'_n = \sum_{j=1}^{N_x} D_3 U_s(x_k; x_j, f_j) \sum_{n=1}^{N_\alpha} (D_{\alpha_n} f_j) \alpha'_n$$

$$G_{k,n}(S(t)) = \sum_{j=1}^{N_x} D_3 U_s(x_k; x_j, f_j) D_{\alpha_n} f_j.$$

In the model, particles are joined by spring connections, and the total force applied at a particle location is the sum of the forces due to the springs connected to it, as seen in (6). Hence, $D_{\alpha_n} f_j$ is 0 if the n th spring (with elasticity α_n) is not connected to x_j . Therefore, by defining $v(n)$ to be the set of particles connected by the spring with coefficient α_n , then we obtain

$$G_{k,n}(S(t)) = \sum_{j \in v(n)} D_3 U_s(x_k; x_j, f_j) D_{\alpha_n} f_j. \quad (16)$$

By identification of the coefficients of x'_i between (10) and (11), it can be concluded as shown in the equation at the bottom of the page. Then

$$F_{k,n}(S(t)) = \sum_{i=0}^3 D_1 U_r(x_k; x_{n_i}, L_i) [\text{If } k = n]$$

$$+ D_2 U_r(x_k; x_n, L_n) [\text{If } n \in R]$$

$$+ \sum_{i=0}^3 D_3 U_r(x_k; x_{n_i}, L_i) D_{x_n} L_i [\text{If } n \in R]$$

$$+ \sum_{j=1}^{N_x} D_1 U_s(x_k; x_j, f_j) [\text{If } k = n]$$

$$+ D_2 U_s(x_k; x_n, f_n)$$

$$+ \sum_{j \in c(n)} D_3 U_s(x_k; x_j, f_j) D_{x_n} f_j$$

$$+ D_3 U_s(x_k; x_n, f_n) D_{x_n} f_n \quad (17)$$

where $c(n)$ is the set of particles connected to x_n by some spring. For the last two term we used the fact that $D_{x_n} f_j$ is nonzero only for those forces for which x_n is part of the computation, i.e., the set $c(n) \cup \{x_n\}$.

$$\sum_{n=1}^{N_x} F_{k,n}(S(t))x'_n = \sum_{i=0}^3 \left[D_1 U_r(x_k; x_{n_i}, L_i) x'_k + D_2 U_r(x_k; x_{n_i}, L_i) x'_{n_i} + D_3 U_r(x_k; x_{n_i}, L_i) \sum_{m \in B} (D_{x_m} L_i) x'_m \right]$$

$$+ \sum_{j=1}^{N_x} \left[D_1 U_s(x_k; x_j, f_j) x'_k + D_2 U_s(x_k; x_j, f_j) x'_j + D_3 U_s(x_k; x_j, f_j) \sum_{m=1}^{N_x} (D_{x_m} f_j) x'_m \right]$$

$$D_1 U_r(x_k; x_{n_i}, L_i) = \frac{-\left((6r_{kn_i}^2 + 21\delta^2)L_i \times \frac{(x_k - x_{n_i})}{(r_{kn_i}^2 + \delta^2)^{7/2}} \cdot (x_k - x_{n_i})^T + \frac{(2r_{kn_i}^2 + 5\delta^2)\widehat{L}_i}{(r_{kn_i}^2 + \delta^2)^{5/2}} \right)}{(16\pi)}$$

APPENDIX B

LIST OF DERIVATIVES OF FUNCTIONS

All derivatives required for the previous computations are defined in the following.

Derivatives of Rotlet Component: The expression for the velocity contribution from the rotlet solutions is given in (4) by

$$U_r(x_k; x_{n_i}, L_i) = (2r_{kn_i}^2 + 5\delta^2)L_i \times \frac{(x_k - x_{n_i})}{(16\pi(r_{kn_i}^2 + \delta^2)^{5/2})}$$

where r_{kn_i} is the euclidean distance between x_k and x_{n_i} , and δ is the regularization parameter. Hence, we get the equation at the top of the page, where \widehat{L}_i is the skew symmetric operator $\widehat{\cdot}$ applied to the vector L_i . Also

$$D_2 U_r(x_k; x_{n_i}, L_i) = -D_1 U_r(x_k, x_{n_i}, L_i)$$

$$D_3 U_r(x_k; x_{n_i}, L_i) = -(2r_{kn_i}^2 + 5\delta^2) \frac{(x_k - x_{n_i})}{(16\pi(r_{kn_i}^2 + \delta^2)^{5/2})}$$

Derivatives of Stokeslet Component: The expression for the velocity contribution from the rotlet solutions is given in (4) by

$$U_s(x_k; x_i, f_i) = \frac{(r_{ki}^2 + 2\delta^2)}{8\pi(r_{ki}^2 + \delta^2)^{3/2}} f_i + \frac{[f_i^T(x_k - x_i)]}{8\pi(r_{ki}^2 + \delta^2)^{3/2}} (x_k - x_i).$$

Hence

$$\begin{aligned} D_1 U_s(x_k; x_i, f_i) &= -\frac{(r_{ki}^2 + 4\delta^2)}{8\pi(r_{ki}^2 + \delta^2)^{5/2}} f_i (x_k - x_i)^T \\ &\quad + \frac{1}{8\pi(r_{ki}^2 + \delta^2)^{3/2}} (x_k - x_i) f_i^T \\ &\quad - \frac{3[f_i^T(x_k - x_i)]}{8\pi(r_{ki}^2 + \delta^2)^{5/2}} (x_k - x_i)(x_k - x_i)^T \\ &\quad + \frac{[f_i^T(x_k - x_i)]}{8\pi(r_{ki}^2 + \delta^2)^{3/2}} I \\ D_2 U_s(x_k; x_i, f_i) &= -D_1 U_s(x_k, x_i, f_i) \\ D_3 U_s(x_k; x_i, f_i) &= \frac{(r_{ki}^2 + 2\delta^2)I}{(8\pi(r_{ki}^2 + \delta^2)^{3/2})} + \frac{(x_k - x_i)(x_k - x_i)^T}{(8\pi(r_{ki}^2 + \delta^2)^{3/2})}. \end{aligned}$$

Derivatives of the Torques: The torques, as given in (7), are defined as: $L_i = \sigma_i p / \|p\|$, where $p \triangleq (x_{n_0} - (x_{n_1} + x_{n_2} + x_{n_3})/3)$, σ_i is the magnitude of the torque, $n_j \in R$ are the indexes of the points used for computing the direction of the torque and where the torques are applied.

Clearly, if $k \notin R$ then $D_{x_k} L_i = 0$. In the case that $k = n_0$, then

$$D_{x_{n_0}} L_i = \sigma_i \frac{I}{\|p\|} - \sigma_i \frac{pp^T}{\|p\|^3}.$$

Also, $D_{x_{n_1}} L_i = D_{x_{n_2}} L_i = D_{x_{n_3}} L_i = -(1/3)D_{x_{n_0}} L_i$.

Derivatives of the Forces: The forces are also defined in (6) as

$$f_i = \sum_{n \in c(i)} \alpha_{in} \left(1 - \frac{r_{0,in}}{r_{in}} \right) (x_n - x_i)$$

where α_{in} is the elasticity constant between x_n and x_i , and $r_{0,in}$ is the rest length between x_n and x_i .

Clearly, if $k \notin c(i)$ and $k \neq i$ then $D_{x_k} f_i = 0$. Otherwise, for $k \in c(i)$

$$D_{x_k} f_i = \alpha_{ik} \left(\frac{r_{0,ik}}{r_{ik}^3} \right) (x_k - x_i)(x_k - x_i)^T + \alpha_{ik} \left(1 - \frac{r_{0,ik}}{r_{ik}} \right) I$$

$$D_{x_i} f_i = - \sum_{k \in c(i)} D_{x_k} f_i.$$

We also have that

$$D_{\alpha_{in}} f_i = \left(1 - \frac{r_{0,in}}{r_{in}} \right) (x_n - x_i)$$

for α_{in} connecting x_n to x_i . In general, if α_k does not connect any node to x_i , then $D_{\alpha_k} f_i = 0$.

ACKNOWLEDGMENT

The authors would like to thank R. Cortez for his feedback and input in this work. They would also like to thank J. Hsia for his collaboration in this work.

REFERENCES

- [1] B. R. Donald, C. Levey, C. McGray, I. Paprotny, and D. Rus, "An untethered, electrostatic, globally controllable mems micro-robot," *J. Microelectromech. Syst.*, vol. 15, pp. 1–15, 2006.
- [2] K. B. Yesin, K. Vollmers, and B. J. Nelson, "Modeling and control of untethered biomicrobots in a fluidic environment using electromagnetic fields," *Int. J. Robot. Res.*, vol. 25, no. 5–6, pp. 527–536, 2006.
- [3] H. Li, J. Tan, and M. Zhang, "Dynamics modeling and analysis of a swimming microrobot for controlled drug delivery," in *Proc. IEEE Int. Conf. Robot. Autom. (ICRA)*, 2006, pp. 1768–1773.
- [4] J. P. Armitage and R. Schmitt, "Bacterial chemotaxis: Rhodospirillum rubrum and sinorhizobium meliloti—Variations on a theme?," *Microbiology*, vol. 143, pp. 3671–3682, 1997.
- [5] J. P. Armitage, T. P. Pitta, M. A. Vigeant, H. L. Packer, and R. M. Ford, "Transformations in flagellar structure of rhodospirillum rubrum and possible relationship to changes in swimming speed," *J. Bacteriology*, vol. 181, no. 16, pp. 4825–4833, 1999.
- [6] H. Flores, E. Lobaton, S. Mendez-Diez, S. Tlupavova, and R. Cortez, "A study of bacterial flagellar bundling," *Bulletin Math. Biol.*, vol. 67, pp. 137–168, 2005.
- [7] E. M. Purcell, "The efficiency of propulsion by a rotating flagellum," *Proc. Nat. Acad. Sci.*, vol. 94, pp. 11307–11311, 1997.
- [8] A. Najafi and R. Golestanian, "Simple swimmer at low reynolds number: Three linked spheres," *Phys. Rev. E*, vol. 69, pp. 062901–062904, 2004.
- [9] R. Dreyfus, J. Baudry, M. L. Roper, M. Fermigier, H. A. Stone, and J. Bibette, "Microscopic artificial swimmers," *Nature*, vol. 437, no. 6, pp. 862–865, 2005.

- [10] J. J. H. Long, A. C. Lammert, C. A. Pell, M. Kemp, J. A. Strother, H. C. Cheenshaw, and M. J. McHenry, "A navigational primitive: Biorobotic implementation of cycloptic helical klinotaxis in planar motion," *IEEE J. Oceanic Eng.*, vol. 29, no. 3, pp. 795–806, Jul. 2004.
- [11] N. Darnton, L. Turner, K. Breuer, and H. Berg, "Moving fluid with bacterial carpets," *Biophys. J.*, vol. 86, pp. 1863–1870, 2004.
- [12] S. Martel, C. Tremblay, S. Ngakeng, and G. Langlois, "Controlled manipulation and actuation of micro-objects with magnetotactic bacteria," *Appl. Phys. Lett.*, vol. 89, p. 233904, 2006.
- [13] B. Behkam and M. Sitti, "Design methodology for biomimetic propulsion of miniature swimming robots," *ASME J. Dyn. Syst., Meas., Control*, vol. 128, no. 1, pp. 36–43, 2006.
- [14] B. Behkam and M. Sitti, "Bacterial flagella-based propulsion and on/off motion control of microscale objects," *Appl. Phys. Lett.*, vol. 90, p. 023902, 2007.
- [15] D. Steager, C. Kim, J. Patel, S. Bith, C. Naik, L. Reber, and M. Kim, "Control of microfabricated structures powered by flagellated bacteria using phototaxis," *Appl. Phys. Lett.*, vol. 90, p. 263901, 2007.
- [16] M. Kim and T. Powers, "Deformation of a helical filament by flow and electric or magnetic fields," *Phys. Rev. E (Statistical, Nonlinear, Soft Matter Phys.)*, vol. 71, no. 2, p. 021914, 2005.
- [17] B. Qian, T. Powers, and K. Breuer, "Shape transition and propulsive force of an elastic rod rotating in a viscous fluid," *Phys. Rev. Lett.*, vol. 100, no. 7, p. 78101, 2008.
- [18] S. Lim and C. Peskin, "Simulations of the whirling instability by the immersed boundary method," *SIAM J. Scientific Comput.*, vol. 25, no. 6, pp. 2066–2083, 2004.
- [19] R. Cortez, L. Fauci, and A. Medovikov, "The method of regularized stokeslets in three dimensions: Analysis, validation, and application to helical swimming," *Phys. Fluids*, vol. 17, p. 031504, 2005.
- [20] R. L. Raffard, K. Amonlirdviman, J. D. Axelrod, and C. J. Tomlin, "Automatic parameter identification via the adjoint method, with application to understanding planar cell polarity," in *Proc. 45th IEEE Conf. Decision Control*, San Diego, CA, Dec. 2006, pp. 13–18.
- [21] K. Amonlirdviman, N. A. Khare, D. R. P. Tree, W. S. Chen, J. D. Axelrod, and C. J. Tomlin, "Mathematical modeling of planar cell polarity to understand domineering nonautonomy," *Science*, vol. 307, no. 3, pp. 423–426, 2005.
- [22] A. Jameson, "Aerodynamic design via control theory," *J. Scientific Comput.*, vol. 3, no. 3, pp. 233–260, 1988.
- [23] T. R. Bewley, "Flow control: New challenges for a new renaissance," *Progress Aerosp. Sci.*, vol. 37, pp. 21–58, 2001.
- [24] O. M. Aamo and M. Krstic, *Flow Control by Feedback*. New York: Springer-Verlag, 2002.
- [25] D. Jacquet, M. Krstic, and C. C. de Wit, "Optimal control of scalar one-dimensional conservation laws," in *Proc. Amer. Control Conf.*, Minneapolis, MN, Jun. 2006, pp. 2499–2504.
- [26] A. M. Bayen, R. Raffard, and C. J. Tomlin, "Adjoint-based control of a new Eulerian network model of air traffic flow," *IEEE Trans. Control Syst. Technol.*, vol. 14, no. 5, pp. 804–818, Sep. 2006.
- [27] M. Nodet, "Variational assimilation of lagrangian data in oceanography," *Inverse Problems*, vol. 22, no. 1, pp. 245–263, 2006.
- [28] D. Sun, I. Strub, and A. Bayen, "Comparison of the performance of four eulerian network flow models for strategic air traffic management," *Netw. Heterogeneous Media*, vol. 2, no. 4, pp. 569–594, 2007.